

Magnetization process in a chiral p -wave superconductor with multi-domains

Masanori Ichioka,* Yasushi Matsunaga, and Kazushige Machida
Department of Physics, Okayama University, Okayama 700-8530, Japan
 (Dated: November 9, 2018)

A simulation study for the magnetization process is performed for the multi-domain state in a chiral p -wave superconductor, using the time-dependent Ginzburg-Landau theory. The external field penetrates inside as core-less vortices through the domain wall, forming the vortex sheet structure. We find that, with increasing magnetic fields, the domain walls move so that the unstable domains shrink to vanish. Therefore, the single domain structure is realized at higher fields.

PACS numbers: 74.25.Qt, 74.20.Rp, 74.20.De, 74.70.Pq

A quasi-two dimensional superconductor Sr_2RuO_4 is an unconventional superconductor, and the pairing symmetry is suggested to be a chiral p -wave pairing with the basic form $p_{\pm} = p_x \pm ip_y$ and in-plane equal-spin pairing.^{1,2} The spin-triplet pairing is supported by the fact that the Knight shift does not change below the superconducting transition temperature T_c .³ Since the spontaneous moment appears below T_c in the observation of the muon spin relaxation (μSR), time-reversal symmetry of the pairing function is broken.⁴ The internal field distribution of the vortex state, which is observed by a small angle neutron scattering (SANS), is consistent to the chiral p -wave pairing state.⁵ While the pairing function of Sr_2RuO_4 may have an additional horizontal node, such as $(p_x \pm ip_y) \cos p_z$,⁶ it is intrinsic in our study that the pairing function has a factor of the chiral component $p_x \pm ip_y$.

In the chiral p -wave superconductor, a p_+ state and a p_- state are degenerate in free energy. Therefore, the multi-domain structure may realize, i.e., some regions in a sample are p_+ domains and others are p_- domains. Between the p_+ and p_- domains, domain walls appear as topological defects, which are not easily destroyed.^{7,8} In the vortex state when a magnetic field \mathbf{H} is applied to \hat{z} direction, the degeneracy of the p_+ and p_- states is removed. When $\mathbf{H} \parallel \hat{z}$ and charge $e > 0$ (or equivalently when $\mathbf{H} \parallel -\hat{z}$ and $e < 0$), the free energy of the p_- state is lower than that of the p_+ state,⁹ because the vortex structures are different between the p_+ and p_- domains. In the p_- (p_+) state, the opposite p_+ (p_-) component induced around the vortex core has large (small) amplitude.^{9,10,11} Since the p_- state is stable in the vortex state, it is interesting to see how the multi-domain structure at a zero field changes to the single p_- domain, when a magnetic field is applied. We note that the chirality dependence is defined relative to the magnetic field direction, the free energy of the p_+ state becomes smaller when the magnetic field is applied to the reverse direction $-\hat{z}$. Study of vortices trapped at the domain wall is also important since they are considered to have a strange structure called a “vortex sheet”,¹² where half flux-quantum vortices are aligned along the domain wall.^{8,13,14,15,16}

The purpose of this paper is to study the magnetization process in order to understand how the multi-domain structure changes to the single p_- domain by

applying magnetic fields in the chiral p -wave superconductor. We also investigate the roles and properties of the vortex sheet structure at the domain wall appearing in the magnetization process. The static properties of the vortex or domain wall structure were studied also by the two-component Ginzburg-Landau (GL) theory.^{7,8,10,17,18} For the study of the magnetization process, we use the time-dependent Ginzburg-Landau (TDGL) theory as a phenomenological approach in our qualitative study, with expectation that vortices move so as to approach the free energy minimum state. The magnetization process of a conventional superconductor was studied by Kato *et al.*^{19,20} The present authors studied the static and dynamical properties of the vortex sheet structure in a two-component superconductor based on the TDGL theory.^{13,14} In this paper, we use the GL free energy for the chiral p -wave superconductor, and study the magnetization process.

To obtain the two-component GL equation in the chiral p -wave superconductor, the pair potential is decomposed as $\Delta(\mathbf{r}, \mathbf{p}) = \eta_+(\mathbf{r})\phi_+(\mathbf{p}) + \eta_-(\mathbf{r})\phi_-(\mathbf{p})$ with the order parameter $\eta_{\pm}(\mathbf{r})$, where \mathbf{r} is the center-of-mass coordinate of the Cooper pair. The pairing functions $\phi_{\pm}(\mathbf{p})$, depending on the relative momentum \mathbf{p} of the pair, are given by the chiral p -wave type such as $p_x \pm ip_y$. The GL free energy density is written as

$$\begin{aligned} \tilde{f} = & - \left(1 - \frac{T}{T_c} \right) (|\eta_+|^2 + |\eta_-|^2) + \frac{1}{2}|\eta_+|^4 + \frac{1}{2}|\eta_-|^4 \\ & + 2|\eta_+|^2|\eta_-|^2 + C_1 (\eta_+^{*2}\eta_+^2 + \eta_-^{*2}\eta_-^2) + \eta_+^* (q_x^2 + q_y^2)\eta_+ \\ & + \eta_-^* (q_x^2 + q_y^2)\eta_- + C_2 (\eta_+^* q_-^2 \eta_- + \eta_-^* q_+^2 \eta_+) \\ & + C_3 (\eta_+^* q_+^2 \eta_- + \eta_-^* q_-^2 \eta_+) \end{aligned} \quad (1)$$

in the dimensionless form,¹³ where $q_{\pm} = q_x \pm iq_y$, $\mathbf{q} = (\hbar/i)\nabla - 2\pi(2e/\hbar c)\mathbf{A}$ with vector potential \mathbf{A} . $\hbar c/2|e| = \phi_0$ is a flux-quantum. The coefficients are related to the pairing function and the Fermi surface structure as

$$\begin{aligned} C_1 &= \frac{\langle \phi_-^{*2} \phi_+^2 \rangle}{2\langle |\phi_+|^4 \rangle}, \quad C_2 = \frac{\langle v_+^2 \phi_+^* \phi_- \rangle}{2\langle v_+ v_- |\phi_+|^2 \rangle}, \\ C_3 &= \frac{\langle v_-^2 \phi_+^* \phi_- \rangle}{2\langle v_+ v_- |\phi_+|^2 \rangle}, \end{aligned} \quad (2)$$

where $v_{\pm} = (v_x \pm iv_y)/2$ with a Fermi velocity (v_x, v_y) , and $\langle \cdots \rangle$ indicates the average on \mathbf{p} along the Fermi sur-

face. C_1 and C_3 are anisotropy parameters which are finite when the pairing functions or the Fermi surface have fourfold symmetric structure. For the isotropic case, $C_1 = C_3 = 0$ due to the vanishing Fermi surface average in Eq. (2). As the detailed forms of ϕ_{\pm} and the Fermi surface structure have not been established yet, we treat the coefficients in Eq. (2) as arbitrary parameters. In this study we set $C_1 = C_3 = 0$ for simplicity to exclude the additional anisotropy effect. We show results calculated for $C_2 = 0.3$ and $T = 0.5T_c$.

In our simulations, we use the TDGL equation coupled with Maxwell equations,^{19,20}

$$\frac{\partial}{\partial t}\eta_1 = -\frac{1}{12}\frac{\partial \tilde{f}}{\partial \eta_1^*}, \quad \frac{\partial}{\partial t}\eta_2 = -\frac{1}{12}\frac{\partial \tilde{f}}{\partial \eta_2^*}, \quad (3)$$

$$\frac{\partial}{\partial t}\mathbf{A} = \tilde{\mathbf{j}}_s - \kappa^2 \nabla \times \mathbf{B}, \quad \mathbf{B} = \nabla \times \mathbf{A}. \quad (4)$$

The supercurrent $\tilde{\mathbf{j}}_s = (\tilde{j}_{s,x}, \tilde{j}_{s,y}) \propto (\partial \tilde{f} / \partial A_x, \partial \tilde{f} / \partial A_y)$ is given by $\tilde{j}_{s,x} = \text{Re}[\eta_+^*(q_x \eta_+) + \eta_-^*(q_x \eta_-) + C_2\{\eta_+^*(q_- \eta_-) + \eta_-^*(q_+ \eta_+)\} + C_3\{\eta_+^*(q_+ \eta_-) + \eta_-^*(q_- \eta_+)\}]$, $\tilde{j}_{s,y} = \text{Re}[\eta_+^*(q_y \eta_+) + \eta_-^*(q_y \eta_-) - iC_2\{\eta_+^*(q_- \eta_-) - \eta_-^*(q_+ \eta_+)\} + iC_3\{\eta_+^*(q_+ \eta_-) - \eta_-^*(q_- \eta_+)\}]$. The length, field, and time are, respectively, scaled by the coherence length ξ_0 , $H_{c2,0} = \phi_0 / 2\pi \xi_0^2$, and $t_0 = 4\pi \xi_0^2 \kappa^2 \sigma / c^2$ with the normal state conductivity σ .^{19,20} However, we here scale η_{\pm} by η_0 instead of $\eta_0(T) = \eta_0(1 - T/T_c)^{1/2}$. η_0 is a uniform solution of η_{\pm} when $\eta_{\mp} = 0$ and $T = 0$. The calculations are performed in a two-dimensional rectangular area with a size $200\xi_0 \times 100\xi_0$. Outside the open boundary, we set $\eta_+ = \eta_- = 0$ and $B(\mathbf{r}) = H$ with an applied field H . We set the GL parameter $\kappa = 2.7$.

Our calculation of the magnetization process for the multi-domain state is shown in Fig. 1. At a zero field, we prepare the state where the right-hand side half region is a p_+ state ($|\eta_+| \sim 1$, $\eta_- = 0$), and the left-hand side half region is a p_- state ($|\eta_-| \sim 1$, $\eta_+ = 0$). A straight domain wall appears at the center between the p_+ and p_- domains. The relative phase of η_+ and η_- is π , which minimizes the free energy in our case. We increase H gradually with a slow rate $\delta H / \delta t = 5 \times 10^{-6}$. The left panels in Fig. 1 show the color-density plot of $|\eta_+(\mathbf{r})|$ and $|\eta_-(\mathbf{r})|$. A green (red) region indicates the p_+ (p_-) domain. The center panels show $|\eta_x(\mathbf{r})|$ and $|\eta_y(\mathbf{r})|$, when we define the p_x component η_x and the p_y component η_y as $\Delta(\mathbf{r}, \mathbf{p}) = \eta_x(\mathbf{r})\phi_x(\mathbf{p}) + \eta_y(\mathbf{r})\phi_y(\mathbf{p})$ with $\phi_x = (\phi_+ + \phi_-)/2 \sim p_x$ and $\phi_y = (\phi_+ - \phi_-)/2i \sim p_y$. Yellow region indicates that $|\eta_x(\mathbf{r})| \sim |\eta_y(\mathbf{r})| \sim 1$ in the p_+ or p_- domains. The right panels represent the internal field distribution $B(\mathbf{r})$, which can be observed directly.

At low fields in the Meissner state [Fig. 1(a)], magnetic fields penetrate inside through the domain wall, forming the vortex sheet structure. A straight domain wall at $H = 0$ begins to meander by the penetration of vortices at finite fields. To see the vortex sheet structure, we show the spatial structure in Fig. 2, magnifying the enclosed area in Fig. 1(a). In the amplitude $|\eta_-(\mathbf{r})|$ and $|\eta_+(\mathbf{r})|$ in Figs. 2(a) and 2(b), we do not see the singularity of the

vortex center. It is because the singularity points with the phase winding 2π of vortices are at the opposite region across the domain wall, where the amplitude of the order parameter is well suppressed. That is, the winding center of η_+ (η_-) is located in the p_- (p_+) domain, as shown by a solid circle in Fig. 2(b) (Fig. 2(a)). Therefore, vortices at the domain wall are core-less vortices.

When we consider η_x and η_y instead of η_+ and η_- , as shown in the center panels in Fig. 1, the core-less vortices of the vortex sheet are seen as different structures. At a zero field, the domain wall is presented as a green line in the color density plot, since $\eta_y \sim 1$ and $\eta_x \sim 0$ due to the sign change of η_x at the domain wall. When the magnetic field penetrates, as shown in the center panel of Fig. 1(a) or in Figs. 2(c) and 2(d), vortices of η_y (red circle) enter along the domain wall from the boundary. These η_y vortices are located slightly at the p_+ domain side in the domain wall region. The green line between the η_y vortices changes to the vortex of η_x (green circle), when an inter-vortices distance of the η_y vortices becomes short with increasing H . That is, the order parameters η_x and η_y have vortex cores with a winding 2π at different positions. This vortex sheet structure with the η_x and η_y vortices alternately aligning along the domain wall is the same vortex sheet structure reported in our previous work.^{13,14} The $B(\mathbf{r})$ distribution has a ridge along the domain wall, and has a peak at the η_y vortices, as shown in the right panel of Fig. 1(a) or in Fig. 2(e).

With increasing H , first, vortices penetrate inside only in the p_- domain [Fig. 1(b)]. Later at higher field, vortices penetrate also in the p_+ domain [Fig. 1(c)]. These indicate that the lower critical field H_{c1} in the p_- domain is lower than that in the p_+ domain. This corresponds to the fact that the upper critical field H_{c2} in the p_- state is higher than that of the p_+ state.⁹ The amplitude of the induced p_+ component around vortices in the p_- state is larger than that of the induced p_- component in the p_+ state.⁹ Since H_{c1} is related to the creation energy of the vortex core, therefore, the p_- state with smaller creation energy of the vortex core has smaller H_{c1} compared to the p_+ state.¹⁰ In Figs. 1(b) and 1(c), we see vortices at the boundary region. This is because the penetrating magnetic field decreases towards inside of the superconductor in the length scale of the penetration depth. Near H_{c1} when H increases, vortices first appear at the boundary region where locally $B(\mathbf{r}) > H_{c1}$.

With increasing the number of vortices along the domain wall, the domain wall line moves meanderingly. With further increasing H , the domain wall moves so that the area of the p_+ domain shrinks as is seen in Fig. 1(d), where the vortex sheet structure still appears along the meandering domain wall. Finally at enough high fields, the p_+ domain vanishes, and the single p_- domain state is realized.

Around the vortex cores in the p_+ domain and the p_- domain, the opposite chiral component is induced as discussed in previous works.^{9,10,11} We also observe some double-winding 4π vortex near the boundary regions in

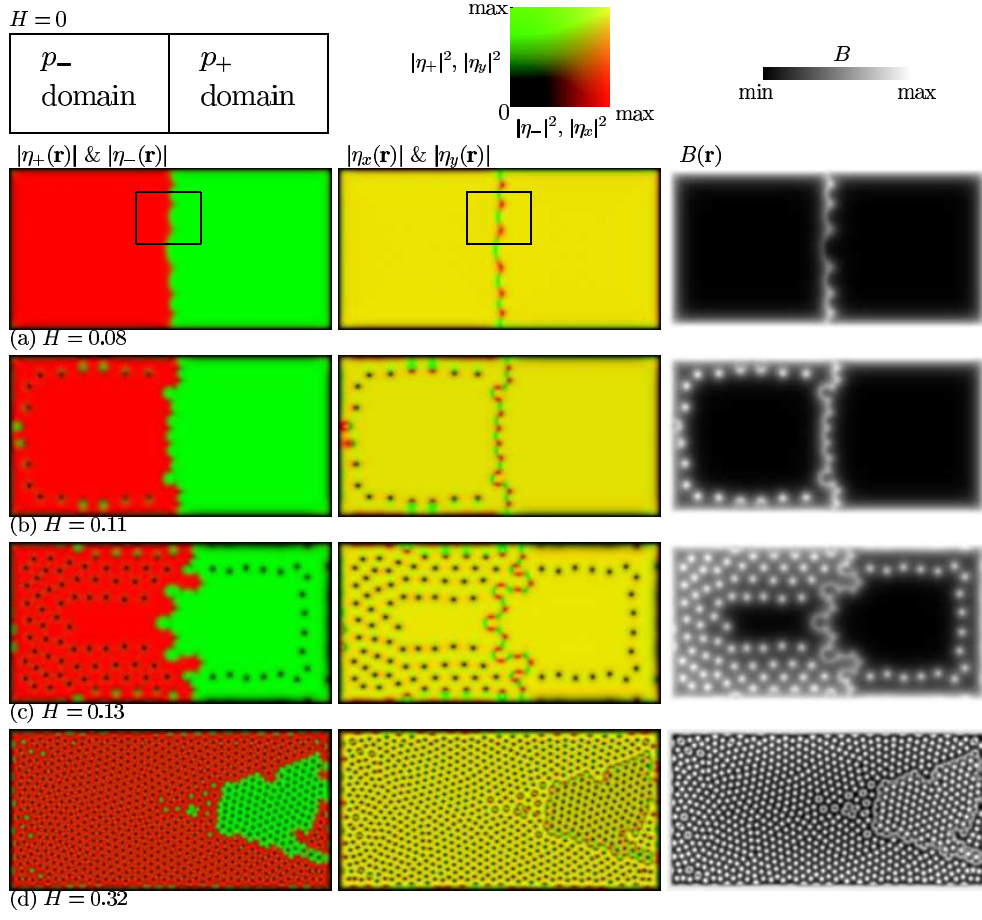


FIG. 1: (Color) Magnetization process for the multi-domain state in a $200\xi_0 \times 100\xi_0$ area with the open boundary. We start from the zero-field state where the left (right) hand side half region is a p_+ (p_-) domain. The applied field H at the boundary is gradually increased. (a) $H/H_{c2,0} = 0.08$, (b) 0.11, (c) 0.13 and (d) 0.32. The left panels show the color density plots of $|\eta_+(\mathbf{r})|$ and $|\eta_-(\mathbf{r})|$. The center panels are for $|\eta_x(\mathbf{r})|$ and $|\eta_y(\mathbf{r})|$. The right panels present the internal field distribution $B(\mathbf{r})$.

the p_- domain. They are seen as large green circles in the red region in the color density plots of $|\eta_+|$ and $|\eta_-|$ in Figs. 1(b)-1(d), since the vortex core of the double-winding vortex in the η_- component is filled by the induced η_+ component with a winding 0. The population of the double-winding vortex increases with increasing C_2 , which is the strength of the gradient coupling between the p_+ and p_- components. In the $B(\mathbf{r})$ distribution, the double-winding vortex has a local minimum of $B(\mathbf{r})$ at the vortex center within the enhanced $B(\mathbf{r})$ region around the vortex core, due to the induced η_+ component. Because this $B(\mathbf{r})$ structure is not consistent to that observed by SANS,⁵ however, most of the vortices in Sr_2RuO_4 are not double-winding vortices.

We also examine the single domain case of a p_+ state at $H = 0$. Since the p_- state has lower free energy in the vortex state, the p_+ domain has to change to the p_- domain by applying fields. With increasing H , vortices penetrate inside in the single p_+ domain at $H \sim 0.11$. At a higher field $H \sim 0.25$, some small p_- domains are created at the boundary. With further increasing H , the area of the p_- domain extends inside, as shown in Fig.

3. Finally, the p_+ domain shrinks to vanish also in this case, realizing the single p_- domain state.

Lastly, we compare the magnetization curves in Fig. 4 for three cases; (i) the multi-domain case when the p_+ domain and the p_- domain coexist at low fields as shown in Fig. 1, (ii) the case of the single p_+ domain at low fields as shown in Fig. 3, and (iii) the case of the single p_- domain. In the single domain case, $B = 0$ in the Meissner state at $H < H_{c1}$, and B appears in the mixed state at $H > H_{c1}$ due to the penetration of vortices. We find that $H_{c1}(p_- \text{ state}) < H_{c1}(p_+ \text{ state})$ also in Fig. 4. In the multi-domain case (thin solid line in Fig. 4), B is small but finite even in the Meissner state, because the magnetic field penetrates along the domain wall. In this case, the slope of B curve changes both at $H_{c1}(p_+ \text{ state})$ and at $H_{c1}(p_- \text{ state})$.

In summary, we performed the simulation of the magnetization process in a chiral p -wave superconductor, using the TDGL theory with two components of the p_+ and p_- states. In the multi-domain case of the p_+ and p_- domains, the magnetic field penetrates as core-less vortices along the domain wall, forming the vortex sheet

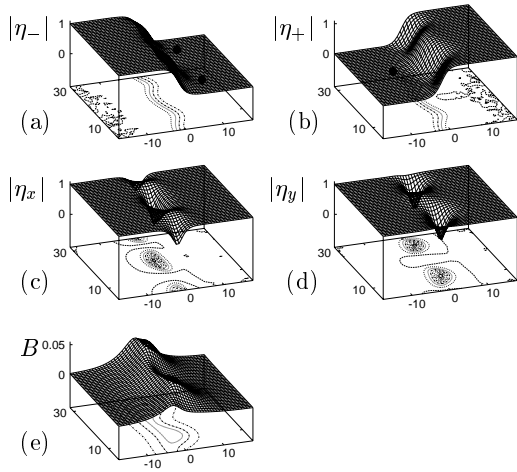


FIG. 2: Vortex sheet structure at $H/H_{c2,0} = 0.08$ in the enclosed area in Fig. 1(a). (a) $|\eta_{-}(\mathbf{r})|$, (b) $|\eta_{+}(\mathbf{r})|$, (c) $|\eta_x(\mathbf{r})|$, (d) $|\eta_y(\mathbf{r})|$, and (e) $B(\mathbf{r})$ are presented. Solid circles in (a) and (b) indicate the position of a phase winding 2π for $\eta_{-}(\mathbf{r})$ and $\eta_{+}(\mathbf{r})$, respectively.

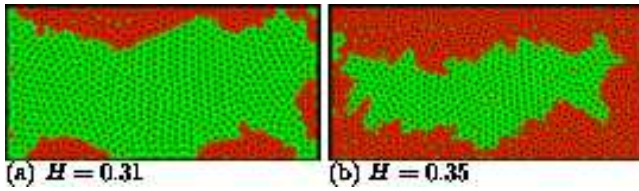


FIG. 3: (Color) Magnetization process in the single domain case of a p_{+} state at $H = 0$. Color density plots of $|\eta_{+}(\mathbf{r})|$ and $|\eta_{-}(\mathbf{r})|$ are presented at (a) $H/H_{c2,0} = 0.31$, and (b) 0.35.

structure, even in the Meissner state. With increasing

external fields, the domain wall meanderingly moves, so that the area of the p_{+} domain shrinks. Then, the unstable p_{+} domain vanishes at a high field, and the single domain of the stable p_{-} state is realized. Even in the case of the single p_{+} domain at a zero field, the p_{+} domain changes to the single p_{-} domain at a high field as in a similar way, after small p_{-} domains are created at the boundary.

Recently, anomalous internal field distribution due to the vortex coalescence was observed.²¹ These may be related to the intrinsic character of the chiral p -wave superconductor, such as a domain structure.

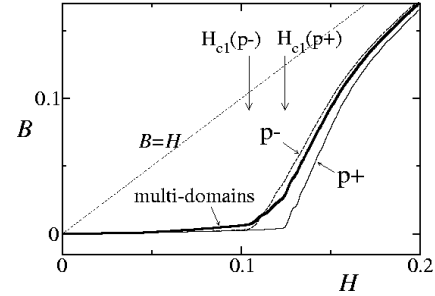


FIG. 4: Magnetization curve at low fields. Averaged flux density B is plotted as a function of an external field H . We normalize H and B by $H_{c2,0}$. When the spatial average B is calculated from $B(\mathbf{r})$, we exclude the boundary region of the width $10\xi_0$ not to consider the surface effect at the sample boundary. A thin solid line is for the multi-domain case shown in Fig. 1. A thick solid (dashed) line is for the single domain case when we start from a single p_{+} (p_{-}) domain at $H = 0$. The dash-dotted line shows $B = H$.

* Electronic address: oka@mp.okayama-u.ac.jp

¹ Y. Maeno, H. Hashimoto, K. Yoshida, S. Nishizaki, T. Fujita, J.G. Bednorz, and F. Lichtenberg, *Nature* **372**, 532 (1994).

² T.M. Rice and M. Sigrist, *J. Phys.: Cond. Matter* **7**, L643 (1995).

³ K. Ishida, H. Mukuda, Y. Kitaoka, K. Asayama, Z.Q. Mao, Y. Mori, and Y. Maeno, *Nature* **396**, 658 (1998).

⁴ G.M. Luke, Y. Fudamoto, K.M. Kojima, M.I. Larkin, J. Merrin, B. Nachumi, Y.J. Uemura, Y. Maeno, Z.Q. Mao, Y. Mori, H. Nakamura, and M. Sigrist, *Nature* **394**, 558 (1998).

⁵ P.G. Kealey, T.M. Riseman, E.M. Forgan, L.M. Galvin, A.P. Mackenzie, S.L. Lee, D.McK. Paul, R. Cubitt, D.F. Agterberg, R. Heeb, Z.Q. Mao, and Y. Maeno, *Phys. Rev. Lett.* **84**, 6094 (2000).

⁶ Y. Hasegawa, K. Machida, and M. Ozaki, *J. Phys. Soc. Jpn.* **69**, 336 (2000).

⁷ M. Matsumoto and M. Sigrist, *J. Phys. Soc. Jpn.* **68**, 994 (1999).

⁸ M. Sigrist and D.F. Agterberg, *Prog. Theor. Phys.* **102**, 965 (1999).

⁹ M. Ichioka and K. Machida, *Phys. Rev. B* **65**, 224517 (2002).

¹⁰ R. Heeb and D.F. Agterberg, *Phys. Rev. B* **59**, 7076 (1999).

¹¹ M. Takigawa, M. Ichioka, K. Machida, and M. Sigrist, *Phys. Rev. B* **65**, 014508 (2002).

¹² Ü. Parts, E.V. Thuneberg, G.E. Volovik, J.H. Koivuniemi, V.M.H. Ruutu, M. Heinilä, J.M. Karimäki, and M. Krusius, *Phys. Rev. Lett.* **72**, 3839 (1994).

¹³ Y. Matsunaga, M. Ichioka, and K. Machida, *Phys. Rev. Lett.* **92**, 157001 (2004).

¹⁴ Y. Matsunaga, M. Ichioka, and K. Machida, *Phys. Rev. B* **70**, 100502(R) (2004).

¹⁵ E. Babaev, *Phys. Rev. Lett.* **89**, 067001 (2002).

¹⁶ E. Babaev, L.D. Faddeev, and A.J. Niemi, *Phys. Rev. B* **65**, 100512(R) (2002).

¹⁷ D.F. Agterberg, *Phys. Rev. B* **58**, 14484 (1998).

¹⁸ T. Kita, *Phys. Rev. Lett.* **83**, 1846 (1999).

¹⁹ R. Kato, Y. Enomoto, and S. Maekawa, *Physica C* **227**, 387 (1994).

²⁰ R. Kato, Y. Enomoto, and S. Maekawa, *Phys. Rev. B* **47**, 8016 (1993).

- ²¹ V.O. Dolocan, C. Veauvy, Y. Liu, F. Servant, P. Lejay, D. Mailly, and K. Hasselbach, cond-mat/0406195.